applied nano

MDPI

Article

Copper-Oxide/Aluminum-Oxide-Enhanced Copper-Based Nanocomposites: Assessment of Structural, Mechanical, and Electrical Characteristics

Victor Idankpo Ameh [1], Ojo Friday Abraham [2,3,*] and Benjamin Omotayo Adewuyi [2]

[1] Renewable Energy and Biomass Research, Department of Chemical Engineering, Doornfontein Campus, University of Johannesburg, Johannesburg 2028, South Africa; 222189224@student.uj.ac.za
[2] Department of Metallurgical and Materials Engineering, Federal University of Technology, Akure 340001, Nigeria; boadewuyi@futa.edu.ng
[3] School of Materials Science and Engineering, Colorado State University, Fort Collins, CO 80523, USA
* Correspondence: ojo.abraham@colostate.edu

Abstract

Copper functions as an exceptionally efficient conductor, garnering considerable interest in electrical and thermal applications; however, its relatively malleable nature and insufficient durability may hinder its structural effectiveness. This study focused on the development of copper-based nanocomposites by reinforcing a copper matrix with co-precipitated CuO/Al_2O_3 nanoparticles (varying from 0 to 10 wt% in increments of 2%). A thorough examination was conducted regarding the microstructural characteristics, mechanical properties, and the electrical and thermal conductivities of the composites. X-ray diffraction (XRD) and energy-dispersive spectroscopy (EDS) analysis validated the successful synthesis of nano-sized CuO and Al_2O_3 phases, with an estimated crystallite size of 33.2 ± 2.4 nm. Scanning electron microscopy revealed a relatively uniform distribution of nano-oxides within the copper matrix, albeit with signs of particle agglomeration at higher loading levels. The durability of the copper exhibited a significant enhancement attributed to the nano-oxide reinforcement, achieving an 180% increase relative to pure copper with a 10% reinforcement addition. Consequently, the tensile strength increased by approximately 68% (from around 154 MPa to nearly 260 MPa), while maintaining an exceptional level of ductility. The electrical conductivity of copper remained largely unchanged with the addition of nanoparticles; rather, a slight improvement in conductivity and a ~30% rise in thermal conductivity were observed at the maximum reinforcement level. This research work presents a copper-based nanocomposite that offers remarkable potential for applications requiring enhanced strength, wear resistance, and exceptional electrical and thermal conductivity.

Keywords: copper; aluminum; nanocomposite; mechanical properties; electrical properties

Check for updates

Academic Editor: Giacomo Dacarro

Received: 10 February 2026
Revised: 31 March 2026
Accepted: 7 April 2026
Published: 9 April 2026

Copyright: © 2026 by the authors. Licensee MDPI, Basel, Switzerland. This article is an open access article distributed under the terms and conditions of the Creative Commons Attribution (CC BY) license.

1. Introduction

Pure copper is widely valued for its excellent electrical and thermal conductivities, finding use in applications such as electrical wiring, connectors, heat exchangers, and spot-welding electrodes [1]. However, copper is a relatively soft metal with low yield strength, which limits its use in load-bearing or wear-critical scenarios. Strengthening copper via alloying or work-hardening often comes at the expense of conductivity: an inherent trade-off in copper alloys where increasing strength, such as by solid solution or

precipitation hardening, typically reduces the electrical conductivity [2,3]. For instance, high-strength copper alloys like Cu–Be or Cu–Cr–Zr can achieve tensile strengths in the 500–600 MPa range, but their conductivities are usually only ~70–85% of pure copper [4]. This strength–conductivity trade-off is a long-standing materials challenge.

Dispersing small amounts of a second-phase material into copper is an alternative strategy to enhance mechanical properties while preserving conductivity. Copper matrix composites (CuMCs) reinforced with ceramic particles have attracted considerable attention for this reason [5]. By introducing a hard, thermally stable phase, one can improve hardness, strength, and wear resistance through dispersion strengthening and load transfer, while the continuous copper matrix still provides a conductive network. Among various reinforcement options (oxides like Al_2O_3, SiO_2, and ZrO_2, and carbides/nitrides like SiC, AlN, and TiB_2), aluminum oxide (Al_2O_3) stands out as an attractive candidate for copper [6]. Al_2O_3 (alumina) has a very high melting point, excellent hardness, and chemical inertness, and it is abundant and inexpensive [7]. Even a small volume fraction of fine alumina particles can substantially strengthen copper. Indeed, dispersion-strengthened copper that contains ultra-fine Al_2O_3 formed by internal oxidation achieves significantly improved mechanical properties while retaining conductivity [8].

A major hurdle in making Cu-Al_2O_3 composites by conventional methods is the poor wettability of alumina by molten copper [9]. Directly mixing alumina powder into copper (via stir-casting or powder metallurgy routes) often leads to agglomeration and uneven distribution of particles because the copper melt does not wet Al_2O_3, causing the particles to repel the matrix and cluster or settle due to density differences [10]. This can result in porosity and weak interfaces in the composite. Various processing techniques have been explored to overcome this issue. Ex situ methods (external addition of ceramic) include casting with vigorous stirring or infiltration, powder metallurgy consolidation, and mechanical alloying [11,12]. However, these techniques rely on mechanical dispersion and often require adding wetting agents or coatings to the particles. Most often, a small amount of magnesium (~0.2 wt%) is added to the melt prior to powder addition in the samples, to act as a wetting agent (Mg can react with Al_2O_3 to form MgO and spinel at the interface, improving wetting) [13]. In situ methods generate reinforcement within the copper matrix itself, such as internal oxidation (oxidizing a dilute Al-bearing Cu alloy to form Al_2O_3 in situ), chemical reactions (self-propagating high-temperature synthesis), or chemical methods like sol–gel or co-precipitation of precursor phases [11]. In situ techniques can produce ultra-fine, well-dispersed particles with strong bonding to the matrix. For example, internal oxidation of Cu-Al alloys produces a nanometer-scale dispersion of alumina directly in copper, yielding an oxide-dispersion-strengthened copper with superior strength and good conductivity [12]. Nonetheless, many in situ approaches are complex or costly to scale.

In this study, we employ a hybrid strategy to introduce Al_2O_3 into copper in a way that maximizes dispersion and wetting. We first synthesize a mixed CuO/Al_2O_3 nanopowder via a chemical co-precipitation method. The idea is that CuO intimately mixed with Al_2O_3 can act as an oxygen-bearing carrier for alumina: when this powder is added to molten copper, the CuO may partially reduce to metallic Cu, thereby locally wetting and anchoring the Al_2O_3 particles within the copper matrix [10]. This approach effectively addresses the non-wettability of pure alumina by providing a transient oxide (CuO) that reacts to improve interfacial bonding [8]. The co-precipitated nano-oxides are expected to distribute more uniformly in the cast composite than bare alumina powder additions, as the in situ reduction of CuO can form metallic bridges around alumina and reduce interfacial voids [7]. We reinforce copper with up to 10 wt% of this CuO/Al_2O_3 powder to systematically evaluate the effect on microstructure, hardness, wear, tensile properties,

electrical, and thermal conductivities. However, a detailed microstructural analysis to ascertain the synergistic mechanism of the CuO/Al_2O_3 mixed oxides and the copper matrix was not considered in this work.

2. Materials and Methods

Copper (II) oxide and aluminum oxide mixed nanopowder (CuO/Al_2O_3) was prepared via a chemical co-precipitation technique. Analytical-grade copper (II) nitrate ($Cu(NO_3)_2{\cdot}3H_2O$) and aluminum nitrate ($Al(NO_3)_3{\cdot}9H_2O$) were used as precursor salts. Aqueous solutions of $Cu(NO_3)_2$ and $Al(NO_3)_3$ were mixed in proportions corresponding to an equal volume ratio solution (mixture) of 0.1 M copper nitrate and aluminum nitrate (the overall CuO/Al_2O_3 powder was designed to ensure both phases would be present) [14]. A 0.2 M sodium hydroxide (NaOH) solution was slowly added to the mixed metal nitrate solution under vigorous stirring at room temperature until a precipitate formed at pH ~9–10. The precipitated copper–aluminum hydroxides were aged for 12 h, then filtered and thoroughly washed with deionized water to remove nitrate ions. The washed precipitate was dried overnight at 120 °C. The dried precursor was then calcined in air at 600 °C for 3 h to induce decomposition into oxides. During calcination, the mixed hydroxide/oxide precursor converts into a composite of CuO and Al_2O_3 nanoparticles following Equations (1)–(4). The resulting powder was a fine black/gray powder. X-ray diffraction (XRD) analysis (see Section 3) confirmed the presence of crystalline CuO and α-Al_2O_3 phases in this powder.

$$Cu(NO_3)_{2(aq)} + 2NaOH_{(aq)} \rightarrow Cu(OH_2)_{(s)} + 2NaNO_{3(aq)} \quad (1)$$

$$Cu(OH)_2 \xrightarrow{Heat} CuO + H_2O \quad (2)$$

$$Al(NO_3)_{3(aq)} + 3NaOH_{(aq)} \rightarrow Al(OH_3)_{(s)} + 3NaNO_{3(aq)} \quad (3)$$

$$2Al(OH)_3 \xrightarrow{Heat} Al_2O_3 + 3H_2O \quad (4)$$

The CuO/Al_2O_3 powder was used to reinforce a copper matrix via casting. Commercial high-purity copper (electrolytic tough pitch copper scrap, >99.5% Cu) was melted in a graphite crucible using an induction furnace. Once the copper melt reached ~1200 °C, a measured quantity of CuO/Al_2O_3 powder was added to achieve the desired weight percentage (0, 2, 4, 6, 8, and 10 wt% reinforcements were prepared). The molten mixture was mechanically stirred using a graphite impeller at ~500 rpm for 5 min to disperse the particles. After stirring, the composite melt was poured into sand molds to cast cylindrical ingots (approximately 20 mm diameter × 150 mm length). The casting and solidification were conducted under a protective charcoal flux cover to minimize oxidation of the copper. For the unreinforced reference (0%), pure copper was cast under the same conditions (without powder addition).

Phase identification of the synthesized nanocomposite powder was carried out by X-ray diffraction (XRD). Powder XRD patterns were collected on a PANalytical diffractometer with Cu Kα radiation (λ = 1.5406 Å), operating at 40 kV and 30 mA. Scans were taken over 2θ = 20–80° at a 0.02° step size and 1 s dwell per step. The crystallite size of oxide phases was estimated using the Scherrer equation: $D = 0.9\lambda/(\beta \cos\theta)$, where D is the crystallite size, λ the X-ray wavelength, β the full width at half-maximum (FWHM) of a diffraction peak (in radians), and θ the Bragg angle. Key peaks of CuO and Al_2O_3 were analyzed for broadening to calculate D.

Microstructural and elemental fingerprint analysis of the cast composites was performed using scanning electron microscopy-coupled energy-dispersive (SEM-EDS) tech-

niques. Samples were sectioned from the cast rods, mounted in epoxy, and metallographically polished (grit SiC papers followed by 1 μm diamond paste, and a final colloidal silica polish). Selected samples were etched with a dilute ferric chloride solution to reveal copper grain boundaries. SEM imaging was done on a JEOL field-emission SEM at an accelerating voltage of 15 kV. Both secondary electron (SE) and back-scattered electron (BSE) modes were used to visualize the distribution of the oxide particles (the oxides appear bright in BSE mode due to atomic number contrast). Energy-dispersive X-ray spectroscopy (EDS) was performed with TESCAN(Brno; Czech Republic) using a tungsten filament, with a secondary electron detector at 15 mm. EDS using the INCA 7.4 software was used to determine elemental composition and in mapping to distinguish the various oxides' distributions in the reinforcement powder. The internal porosity of each sample was measured via Archimedes' principle (ASTM C373): triplicate samples of each composite sample were weighed in air and in distilled water, and the bulk density was calculated. The theoretical density of each composite was also computed from the rule of mixtures (using 8.96 g/cm^3 for Cu and 3.95 g/cm^3 for Al_2O_3) to determine the volume fraction of porosity in the as-cast material.

Hardness was measured using a Brinell hardness tester on the polished cross-sections. The samples were machined to a 10 mm diameter and 10 mm thickness. A 2.5 mm diameter hardened steel ball indenter and a 1225 kgF load were applied, with a dwell time of 10 s. At least five indentations were made per sample, and the average diameter of indents was used to calculate the Brinell Hardness Number (HB). Abrasive wear resistance was evaluated using a Taber abrasion test (ASTM D1044 adapted for metals). Flat disk specimens (diameter ~10 mm, thickness 6 mm) were cut from each composite. The test was performed on a Taber rotary platform abrader with abrasive wheels (Calibrade H-10 wheel, 1 kg load on each wheel). Samples were rotated for 1000 cycles, and mass loss was recorded every 200 cycles. The "wear index" was calculated as the mass loss (in mg) per 1000 cycles, with a lower wear index indicating better wear resistance. Tensile testing was conducted on an Instron universal testing machine to obtain ultimate tensile strength (UTS), elongation, and energy absorption (toughness). Due to the small cast rod diameter, subsize tensile specimens were machined (gauge length 24 mm, diameter 6 mm). Tests were done at room temperature with a strain rate of 1×10^{-3} s^{-1}. An extensometer measured elongation over the gauge length. The 0.2% yield strength was determined by the offset method from the stress–strain curve.

Electrical resistivity was measured using a four-point probe technique on cast bars of each composite (10 mm × 10 mm × 100 mm). A constant DC current was passed, and the voltage drop measured over a 50 mm central segment to compute resistivity (correcting for the cross-sectional area). Measurements were made at 25 °C; results were reported in Ω·m and converted to conductivity. An eddy-current conductivity meter (Sigma 2008) was also used for a quick verification of conductivity for select samples, which showed consistent values within ±2% of the four-point probe results. Thermal conductivity was determined by a transient plane source (TPS) method using a Hot Disk thermal constant analyzer on disk samples (~50 mm diameter × 5 mm). The thermal conductivity was measured at ~25 °C by placing the sensor between two identical sample disks and using a power/time setting appropriate for the expected range.

3. Results and Discussion

3.1. Microstructure and Elemental Maps of CuO/Al_2O_3 Nanopowder

The XRD pattern of the synthesized CuO/Al_2O_3 powder is shown in Figure 1. Distinct diffraction peaks corresponding to the copper (II) oxide (CuO) and unknown phases are observed, confirming that the co-precipitation and calcination successfully produced a

mixed-oxide powder. The XRD pattern shows strong CuO dominant peaks, with the major CuO peaks appearing at 2θ angles of around ~35.5°, 38.7°, and 48.7°, while α-alumina phases were invariably of low intensity and do not show peak formation. This can be attributed to the high dispersion of CuO on Al_2O_3, causing peak overlap (CuO masking Al_2O_3 peaks), or due to Al_2O_3 amorphization during synthesis in this study. Moreover, it is possible for alumina to exist in transitional phases and processing conditions used during calcination. Nevertheless, the XRD pattern matches well with those reported in the literature for nano CuO and Al_2O_3 mixtures, indicating the expected phase composition [15].

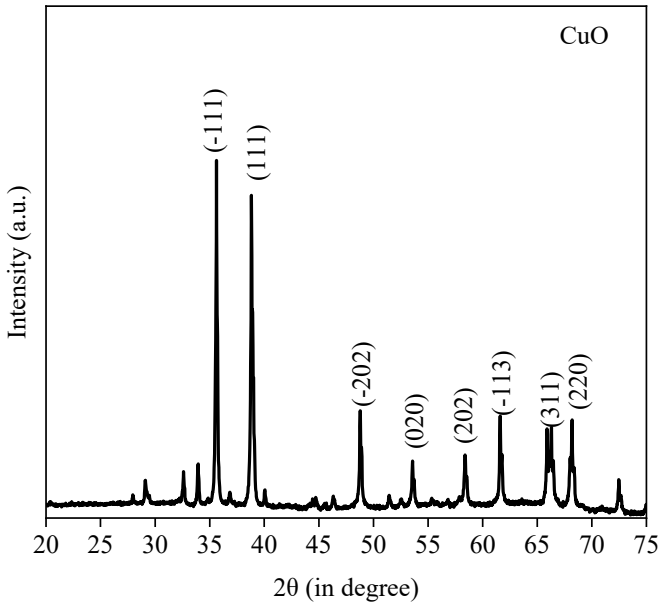


Figure 1. XRD pattern of the CuO/Al_2O_3 mixed-oxide nanopowder, showing peaks of CuO and α-Al_2O_3. The peak broadening is due to the nanoscale crystallite size of the phases.

From the peak broadening analysis using the modified Scherrer formula [16], the average crystallite size of the oxide particles was calculated to be approximately 33.2 ± 2.4 nm. Table 1 lists a few representative diffraction peak positions and the corresponding crystallite size estimates for those peaks. The crystallite size ranged from about 29.4 nm to 36.1 nm for different peaks, and the arithmetic mean was 33.2 nm, with a standard deviation of ±2.4 nm (relative standard deviation of ~7.2%). This confirms that the powder is indeed nanoscaled (with crystallites well below 0.1 μm). The relatively broad peaks, compared to bulk materials, reflect the fine particle size. Note that the Scherrer calculation gives the size of coherent diffracting domains, which in the case of these oxides likely correspond to the individual nano-oxide particles or sub-grains [16]. The presence of both CuO and Al_2O_3 peaks in the pattern validates that the powder contains a mixture of these two oxides as intended. The mixing of CuO and Al_2O_3 at the nanoscale is expected to be beneficial when this powder is introduced into the copper melt, as the CuO can interact with the molten copper and help anchor alumina particles within the metal matrix [17–19].

The copper-based composites were successfully cast for all reinforcement levels (0–10%). The SEM examinations provide insight into the distribution of the CuO/Al_2O_3 particles within the copper matrix. Figure 2a–f present micrographs of the composites corresponding to 0%, 2%, 4%, 6%, 10%, and CuO/Al_2O_3 powder, respectively. In the pure copper sample (Figure 2a), the microstructure is essentially featureless (aside from some polishing scratches and etching pits) with no second-phase particles. In contrast, the reinforced samples show the presence of small discrete particles distributed in the matrix. The nano-oxide particles (being very fine) are not individually resolvable at the magnifica-

tion used, but they appear as clusters or contrast speckles. At 2% and 4% reinforcement (Figure 2b,c), the oxide particles are relatively uniformly dispersed and mostly found at copper grain boundaries or interdendritic regions. In the 4% composite (Figure 2c), some of the pores evident in the 0% Cu (voids from casting) are now occupied by oxide particles (the alumina, being non-wettable by copper, tends to sit in regions where shrinkage porosity might form, effectively filling some voids) [20]. This is corroborated by the density/porosity measurements discussed later—porosity dropped in samples with reinforcement compared to pure copper.

Table 1. XRD peak analysis for CuO/Al_2O_3 powder.

Peak No.	2θ (°)	FWHM (°)	FWHM (Rad)	hkl Plane	Crystallite Size (nm)
1	35.5	0.28	0.00489	(−111)	31.8
2	38.7	0.26	0.00454	(111)	34.5
3	48.9	0.30	0.00524	(−202)	30.2
4	53.6	0.27	0.00471	(020)	33.7
5	58.3	0.25	0.00436	(202)	36.1
6	61.6	0.29	0.00506	(−113)	31.0
7	66.2	0.31	0.00541	(311)	29.4
8	68.4	0.28	0.00489	(220)	32.8
				Average	33.2 ± 2.4 nm

Note: Scherrer constant K = 0.9, Cu Kα radiation.

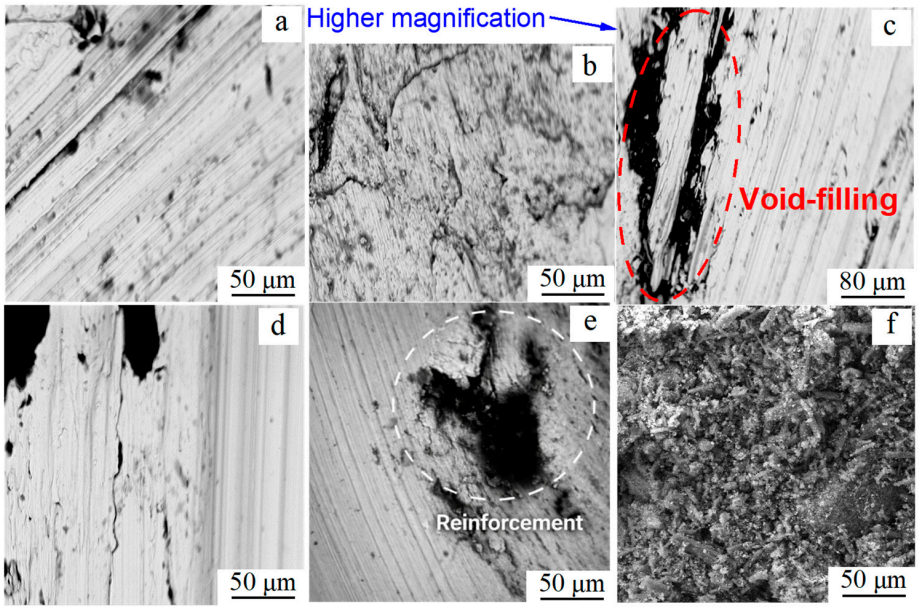


Figure 2. SEM micrographs of copper nanocomposites with (**a**) 0% (unreinforced copper), (**b**) 2%, (**c**) 4%, (**d**) 6%, (**e**) 10%, and (**f**) CuO/Al_2O_3 nanopowders. The 0% sample shows some voids (dark spots) from casting porosity. In the reinforced samples, fine oxide particles (bright speckles) are distributed in the copper matrix (**b**). The 4% sample (**c**) shows voids being filled by particles, and the 10% sample (**e**) shows reinforcement particles' presence. Good particle–matrix interfacial contact is observed in general.

At 6% reinforcement (Figure 2d), the number of particles is higher, and they still seem fairly well distributed, though occasional small agglomerates (particle clusters) begin to appear. By the time the reinforcement reaches 8% and 10%, the micrographs reveal more

pronounced agglomeration of the oxide nanoparticles. In Figure 2e (10% sample), clusters of reinforcement are suspected, and if there are agglomerates present at high loading, the nanoparticles would tend to clump together rather than being perfectly uniformly dispersed. This behavior is expected because as more particles are added, the likelihood of their contacting each other and sintering or clustering during processing increases [21]. Agglomeration can create local stress concentrations and act as crack initiation sites under load, which might offset some benefits of the reinforcement [22,23]. Indeed, as will be seen in the mechanical results, the incremental improvement in properties from 8% to 10% is smaller compared to lower additions, suggesting diminishing returns, possibly due to clustering.

The SEM analysis confirms that the co-precipitated CuO/Al_2O_3 powder was successfully incorporated into the copper matrix. The particles remained mostly well distributed up to moderate loadings and were able to occupy voids, thereby reducing porosity. At the highest reinforcement content, some agglomerations were noted. The microstructural homogeneity achieved by this processing route is quite good relative to many ex situ methods where alumina particles are simply mixed into copper—in those cases, severe segregation or settling can occur due to density differences and poor wetting [24–26]. Here, the presence of CuO, which is likely reduced to metallic Cu during casting, might create local Cu bridges or improved interfaces around the alumina particles, enhancing bonding [27]. No large continuous oxide networks were observed, which is positive because a continuous oxide phase would severely embrittle the material [21]. The oxide seems to be present as discrete second-phase particles within the copper matrix, as depicted in the CuO/Al_2O_3 powder matrix (Figure 2f).

Table 2 and Figure 3 present the energy-dispersive spectroscopy (EDS) spectrum and elemental distribution of the CuO/Al_2O_3 mixed-oxide nanopowder. The analysis confirms the presence of copper, aluminum, and oxygen as the dominant constituents, consistent with the targeted biphasic oxide system. The presence of sodium likely arises from the precursor sodium hydroxide used during material preparations [26]. Morphologically, the EDS-mapped micrograph reveals a relatively uniform dispersion of Al_2O_3 particulates in the copper matrix, a distribution essential for suppressing agglomeration and ensuring improved hardness and conductivity [7,8]. These findings align with earlier reports that CuO/Al_2O_3 nanocomposites exhibit enhanced thermal stability, wear resistance, and electrical performance due to synergistic load transfer and interfacial stabilization mechanisms [10,13]. Overall, the EDS results validate the successful synthesis of a multiphase nanocomposite with potential for structural and functional applications.

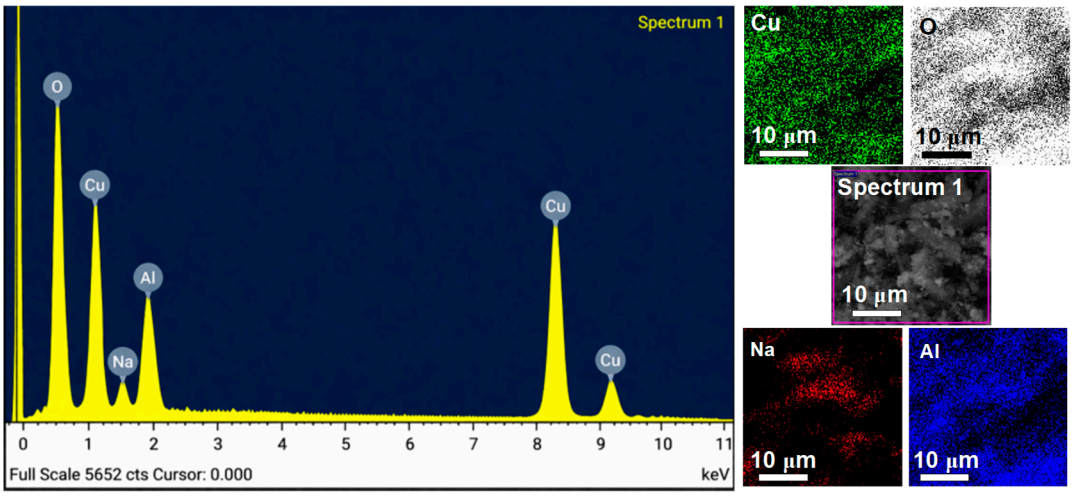


Figure 3. Energy-dispersive spectroscopy of the CuO/Al_2O_3 mixed-oxide nanopowder.

Table 2. Energy-dispersive spectroscopy spectrum elemental analysis.

Element	Weight %	Atomic %
O (K)	39.80	63.10
Na (K)	3.50	3.90
Al (K)	16.20	15.30
Cu (K)	40.50	17.70
Total	100.00	

3.2. Density and Porosity

The densities of the composites were measured to evaluate the presence of porosity. Table 3 summarizes the experimental and theoretical densities for each composition, along with the calculated porosity levels. The pure copper sample (A) had an experimental density (ρ_ex) of 8.62 g/cm^3, which is slightly lower than the theoretical 8.96 g/cm^3 for copper, corresponding to a porosity of about 3.8%. This indicates a small amount of casting porosity in the control copper sample. For the composites, the theoretical density decreases gradually with higher oxide content because Al_2O_3 (3.95 g/cm^3) is much less dense than Cu (8.96 g/cm^3). For example, sample F (10% reinforcement) has a calculated theoretical density (ρ_th) of around 8.58 g/cm^3.

Table 3. Measured density and porosity of pure copper and Cu–CuO/Al_2O_3 composites (values are presented as averages of three replicates, n = 3).

Sample ID	Reinforcement (%)	Experimental Density (g/cm^3)	Theoretical Density (g/cm^3)	Porosity (%)
A	0	8.62	8.96	3.80
B	2	8.75	8.88	1.46
C	4	8.64	8.81	1.93
D	6	8.54	8.73	2.18
E	8	8.52	8.65	1.50
F	10	8.56	8.58	0.23

Note: Theoretical densities computed from the rule of mixtures, using 8.96 g/cm^3 for Cu and 3.95 g/cm^3 for Al_2O_3.

The ρ_ex values for composites B through F show some scatter but are generally close to the theoretical values. Sample B (2% reinforcement) had ρ_ex ≈ 8.75 g/cm^3 vs. the theoretical 8.88 g/cm^3, yielding ~1.5% porosity. Notably, the 10% sample, F, achieved an experimental density of 8.56 g/cm^3, virtually equal to the theoretical 8.58 g/cm^3—corresponding to 0.23% porosity. All composites exhibited porosity under about 2.5%, which is within acceptable ranges for sand–cast metal matrix composites [28]. The trend suggests that introducing nano-oxides may have actually aided the soundness of the casting, perhaps by nucleating solidification and reducing shrinkage pore formation [29]. In particular, the significant drop in porosity at 10% reinforcement (from ~3.8% in pure Cu down to ~0.2%) indicates a much denser microstructure. This aligns with the earlier observation that some voids present in pure copper were filled or mitigated by the presence of the oxide particles (see Figure 2c).

The reduction in porosity with increasing reinforcement also reflects improved casting quality, likely because the dispersed solids restrict the formation of large shrinkage cavities and also because the viscosity of the slurry might increase, slowing down liquid metal contraction [30]. Moreover, the co-precipitated nature of the reinforcement (having some CuO) could promote better wetting of alumina by in situ reduction to Cu at particle surfaces, thereby eliminating interfaces that would otherwise act as voids [31]. The result is that the co-precipitation approach appears to effectively address the non-wettability of pure

alumina in copper by providing a mixed oxide; as a consequence, the composites show very low residual porosity, especially at higher reinforcement contents. All measured porosity values are below 5%, which is generally considered the upper limit for acceptable cast metal composites [32]. The low porosity contributes positively to the mechanical property improvements discussed later.

3.3. Hardness Behavior Trends

Copper in its pure form is very soft (Brinell hardness ~35 HB for annealed copper) [33]. As expected, the addition of hard ceramic nanoparticles led to a significant improvement in the hardness of the copper matrix. The Brinell hardness results for all composite samples are presented in Figure 4. The unreinforced copper (sample A) exhibited a hardness of about 28.4 HB, and with 2 wt% reinforcement (sample B), the hardness increased slightly to 29.8 HB, which is a ~5% increase. At 4% (C) and 6% (D) reinforcement, the hardness rose to 32.9 HB and 38.1 HB, corresponding to 15.9% and 34.1% increases over pure copper, respectively. Notably, at 8% reinforcement (E), the hardness reached 66.4 HB, which is a 133.8% increase—more than double the hardness of pure copper. This trend continued at 10% (F), reaching 79.6 HB, which is 180% higher than the hardness of pure copper.

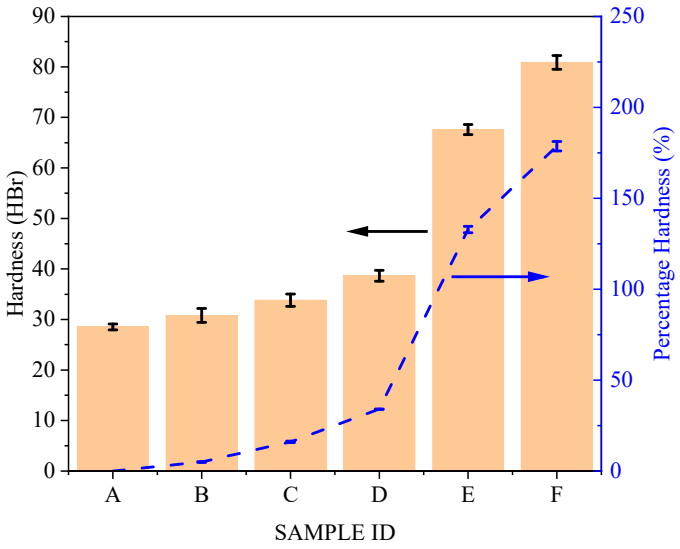


Figure 4. The hardness and percentage increase values relative to pure copper for each composite for samples A–F. These plots clearly illustrate the accelerating improvement at higher reinforcement fractions. At 2% and 4%, the percentage increases are single-digit and mid-teens, whereas at 8% and 10% they leap to triple digits (133% and 180% respectively). The trend suggests that there may be an optimal range around 8–10% where hardness is maximized; adding amounts beyond 10% might not yield further proportional gains since the matrix could become too saturated with particles or introduce defects.

The substantial hardness gain at the higher reinforcement levels indicates the effectiveness of the oxide particles in impeding plastic deformation of the copper matrix [34]. The nanoparticles serve as pinning points to dislocation motion and also load-bearing constituents that inhibit indentation. Even the 8% hardness (66 HB) of the composite exceeds that of many common copper alloys and even rivals the hardness of some brasses [35]. Sample E, with 8% reinforcement, slightly exceeded this value, and sample F (10%) was even higher at ~80 HB. This is a remarkable improvement, essentially transforming copper from a very soft metal to a material with hardness in the range of mild steels [36,37].

The relationship between reinforcement content and hardness appears to be nonlinear. From 0% to 6%, the hardness increase is relatively modest and roughly linear. A substantial rise occurs between 6% and 8%, suggesting a threshold where the dispersion of particles

becomes dense enough to substantially constrain the matrix. It is possible that at ~8% reinforcement, the average interparticle spacing in the microstructure becomes small enough that the copper matrix is effectively an interconnecting network around hard points, rather than a continuous phase with isolated particles [38]. The 10% sample, despite having more agglomeration, still shows an increase over 8%, but the increment (from 66.4 to 79.6 HB) is proportionally smaller than the jump from 6% to 8%. This could indicate that some of the reinforcement in the 10% sample is not as effective due to clustering (suggesting diminishing returns as more particles lump together rather than strengthening separate regions) [38]. Nonetheless, the 10% composite achieved the highest hardness.

The significant hardness improvement can be attributed to multiple strengthening mechanisms introduced by the nano-oxides: dispersion strengthening (oxide particles hinder dislocation motion) [39], grain refinement (the particles can act as nucleation sites during solidification, leading to finer copper grains) [40], and possible Orowan strengthening (dislocations bowing around particles) [41]. Also, as noted earlier, the presence of oxide particles likely reduced casting porosity and defects, indirectly contributing to higher hardness. In essence, the resistance to indentation of the composite is much higher because a portion of the indenting load is borne by the stiff oxide phase, and plastic flow in copper is constrained to smaller regions between particles [39].

3.4. Abrasive Wear Resistance and Tensile Properties

The wear performance of the composites, expressed as the wear index (weight loss per 1000 cycles), improved markedly with increasing reinforcement. Figure 5a shows the Taber abrasion test results for all samples. The unreinforced copper (A) had a wear index of 0.702 mg/cycle (this corresponds to a total loss of around 70 mg over 1000 cycles under the given conditions). The addition of 2% CuO/Al_2O_3 (B) reduced the wear index to 0.577 mg/cycle. At 4% reinforcement (C) the wear index further dropped to 0.538, and at 6% (D) it reached 0.452 mg/cycle. This progressive decrease in wear index with reinforcement content indicates that the composite becomes more resistant to abrasion as more hard particles are present to bear the load and protect the copper matrix from wear [42].

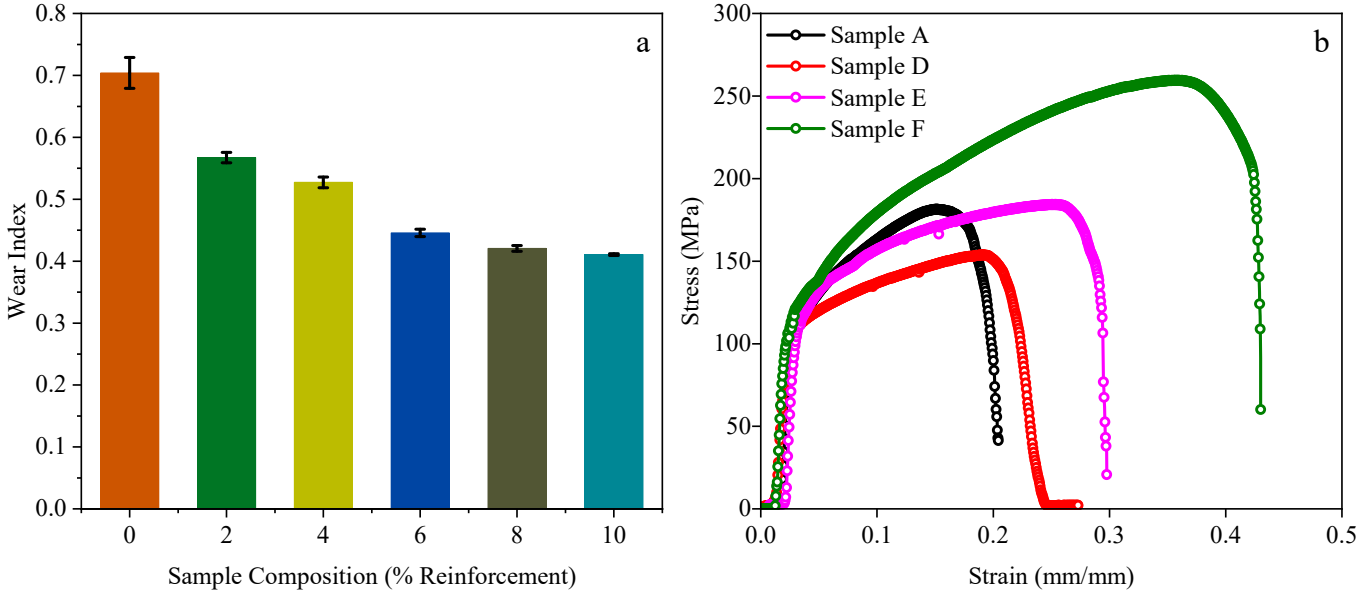


Figure 5. Plots of (**a**) wear index versus reinforcement percentage and (**b**) engineering stress–strain curves for selected samples (0%, 6%, 8%, 10%).

The wear rate reduction from 0% to 10% reinforcement is substantial: the wear index went from 0.702 to 0.409, which is about a 42% decrease. In other words, the 10% reinforced composite lost only ~58% of the material that pure copper did under the same wear test, effectively almost doubling the wear life. This trend correlates strongly with the hardness results—harder materials typically exhibit better wear resistance under abrasive conditions, following Archard's law (wear volume is inversely related to hardness, for a given set of conditions) [43]. The oxide particles act as micro-scale hard "grit" distributed in the matrix; during the abrasion test, they help carry some of the contact load, thereby reducing the wear of the copper itself [44]. The copper matrix, being softer, preferentially wears, but as it recedes, more oxide particles come to the surface to shield it, a typical behavior in composite wear known as a self-protecting mechanism [45].

The composite samples outperformed pure copper in wear resistance. Even the 2% composite had an appreciable improvement. This indicates that even a small volume fraction of a hard phase can make a difference in reducing material loss. It is also worth noting that the wear test used (Taber abrasion) involves a combination of rolling/sliding abrasion; in such scenarios ductile metals like copper gall and smear, leading to high mass loss [46]. The presence of the ceramic particles changes the wear mechanism: the composite surface tends to form a mix of metal and ceramic debris, which can sometimes act as a protective tribolayer. The wear surface of the composites was observed to be smoother and covered with fine oxide debris compared to the smeared, torn surface of pure copper. The wear test confirmed that CuO/Al_2O_3 reinforcements significantly enhance the abrasion resistance of copper. The improvement trend aligns with the increase in hardness. The best performance was observed at the highest reinforcement levels, although beyond ~8% the gains were marginal. For practical applications, one might choose a slightly lower reinforcement, 8%, if other factors (like toughness or cost) are considerations, since it achieves nearly the same wear resistance as 10% while avoiding excess agglomeration. The presence of even a small fraction of ceramic phase in copper can shift its wear behavior closer to that of a composite material with dual phases, rather than a pure metal that would suffer severe adhesive/abrasive wear [46].

The tensile behavior of the copper composites was assessed to understand how the addition of the nano-oxides affects strength and ductility. Engineering stress–strain curves for selected samples (0%, 6%, 8%, 10%) are shown in Figure 5b. Pure copper (sample A) exhibited a typical ductile metal response, with yielding and significant plastic deformation before fracture. The UTS of the unreinforced copper was measured at 153.9 MPa, with an elongation to failure of about 27.3% (Table 4). This is in line with properties of cast copper, albeit slightly on the lower side of the expected UTS [47]. The tensile toughness (area under curve) for pure copper was 22.75 MJ/m^3, reflecting the high ductility. With the introduction of CuO/Al_2O_3 particles, the composites displayed notable increases in strength. Table 4 compiles the tensile properties for the pure copper and three composite samples (6%, 8%, 10% reinforcement). The 2% and 4% samples were not tested in tension due to expected intermediate values, so the focus was on the higher reinforcements, where measurable effects were anticipated. Sample D (6% reinforcement) reached a UTS of 181.5 MPa, about 18% higher than that of pure copper. Its modulus was around 12.82 GPa (an improvement, indicating a stiffer material likely due to the ceramic phase, which has a very high elastic modulus) [18]. The elongation of the 6% composite, however, dropped to 20.4%, indicating some loss of ductility. The tensile toughness for this sample was 21.90 MJ/m^3, actually a bit lower than that of pure copper—this is expected because toughness combines strength and ductility, and while strength went up, ductility went down significantly at 6%, leading to a slightly reduced toughness relative to pure Cu [46].

Table 4. Tensile properties of composite samples (values are presented as averages of three replicates, n = 3).

Specimen ID	Reinforcement (%)	Ultimate Tensile Strength (MPa)	Stiffness (E-Modulus) (MPa)	Tensile Toughness (MJ/m^3)	Elongation (%)
A	0	153.9147	10,834.01	22.74725	27.3
D	6	181.4915	12,817.73	21.89752	20.4
E	8	184.3585	13,438.49	34.66271	29.7
F	10	259.5876	14,977.07	69.54910	43.0

For sample E (8% reinforcement), the UTS further increased to 184.4 MPa. The modulus also increased to 13.44 GPa. Interestingly, the elongation rebounded to 29.7%—slightly higher than the pure copper sample's elongation. Its toughness was 34.66 MJ/m^3, which is substantially higher than that of both pure copper and the 6% composite. This combination of improved strength and ductility at 8% is quite remarkable. It suggests that the microstructure and damage mechanisms at 8% reinforcement allowed for extended plasticity (perhaps the particles were effectively arresting micro-cracks and allowing the material to strain more uniformly) [23]. The 8% composite essentially shows the best of both cases: higher strength without sacrificing ductility (in fact, slightly enhancing it). One hypothesis for this behavior is that at around 8% reinforcement, the reduction in porosity plays a big role in improving ductility. With fewer voids, the material can sustain more plastic strain before fracture [30]. Additionally, the particles might promote void nucleation at higher strain, leading to a larger strain-to-failure if those voids coalesce at a later point [39].

The 10% reinforced sample (F) demonstrated the highest UTS, reaching 259.6 MPa, which is approximately a 68% increase over the UTS of pure copper. This is a very significant strengthening effect. The elastic modulus for the 10% sample was about 14.98 GPa, showing the stiffening effect of the ceramic phase [48]. Most surprisingly, the elongation of the 10% composite was 43.0%, which is much higher than that of even the pure copper. Consequently, the toughness reached 69.55 MJ/m^3, roughly three times that of pure copper. This result is intriguing because, typically, adding a brittle phase (ceramics) to a ductile metal tends to reduce ductility, not increase it [18]. The observed increase in ductility at 10% might be partly an experimental anomaly or due to the specifics of our sample (for instance, if the pure copper sample had some undetected flaws that reduced its elongation, whereas the 10% sample had a flawless microstructure aside from the particles). It could also be related to the mechanism of failure: the presence of many particles might have caused micro-voids to form around them, which then allowed the material to undergo extensive uniform elongation [31]. Another factor could be that the 10% sample had the least porosity (only 0.2%), so in effect it behaved like a fully dense material with a distributed second phase, whereas the pure Cu had 3.8% porosity, which likely acted to initiate failure earlier, limiting elongation. Thus, when comparing a fully dense composite to a slightly porous copper, the composite can appear more ductile. This highlights the benefit of the co-precipitation approach not just in strengthening but also in producing high-density material [38].

The general trend across the composites in terms of increased tensile strength with reinforcement alongside the fractured surface is shown in Figure 6. The combination of high strength and good ductility in the 8% and 10% composites is a key finding (Figure 6a). Often, particle-reinforced metal composites suffer from brittleness due to particle cracking or decohesion at the matrix–particle interface [19]. The SEM examination across all fractured tensile specimens (Figure 6b) showed evidence of ductile dimple rupture of the copper matrix along with some voids at particle sites, but no catastrophic particle crack-

ing. The strong bonding between the nano-oxides and the copper matrix likely allowed the composite to deform plastically without premature failure [35]. The co-precipitated CuO/Al_2O_3 reinforcement, having some CuO that possibly reduced to Cu, could form metallic ligaments around alumina that improve interface strength [39].

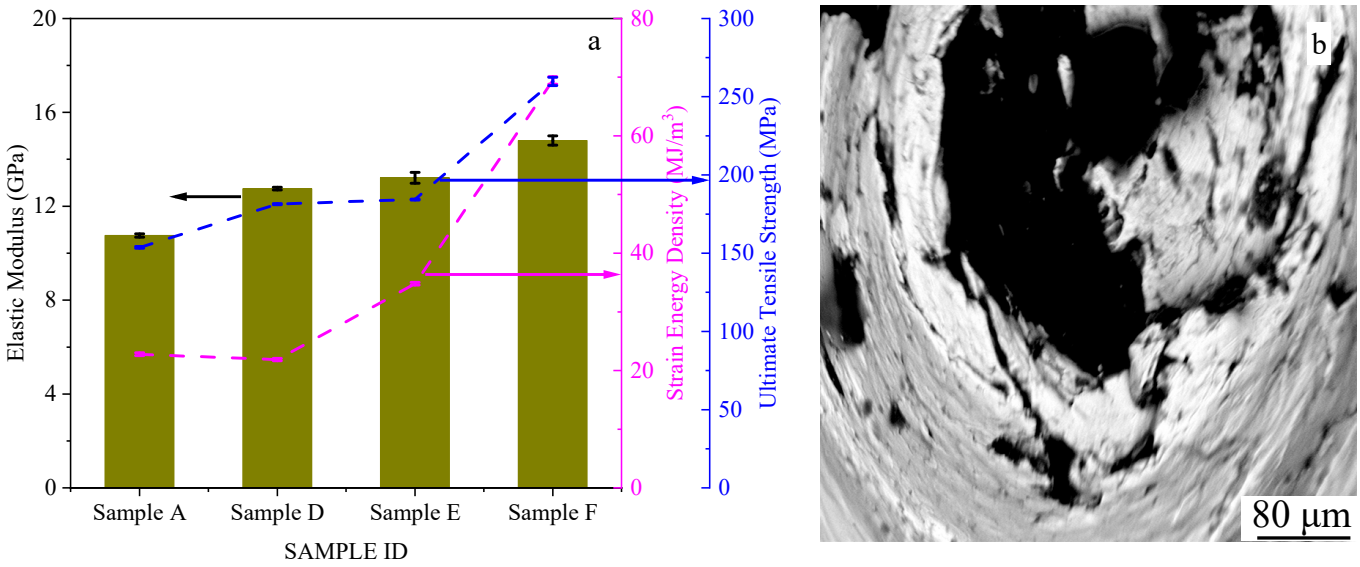


Figure 6. Plots of (**a**) UTS, strain energy density and elastic modulus against composite samples (for the set A, D, E, F) and (**b**) fractured surface of the sample with 10% reinforcement. We observe that UTS stays roughly flat from 6% to 8% and then jumps at 10%. The modulus increases steadily with reinforcement content. Elongation dropped at 6% but then increased at 8% and dramatically at 10%. This non-monotonic ductility behavior underscores the interplay of porosity and particle effects. At 6%, porosity was still ~2.2%, and perhaps stress concentrations at particle clusters initiated cracks early, reducing elongation. By 10%, porosity was negligible, and although there were particle clusters, the sheer number of particles might have caused a more distributed damage mode, allowing higher overall strain.

3.5. Electrical and Thermal Conductivities

One of the primary concerns when adding secondary phases to copper is the potential degradation of electrical and thermal conductivities [49]. The high conductivity of copper is due to its high charge carrier density and low electron scattering; introducing particles (especially non-conductive oxides) might increase electron scattering or reduce the effective cross-section for conduction [50]. In many copper alloys or composites, strength comes at the price of conductivity loss [51,52]. Remarkably, in the present Cu–CuO/Al_2O_3 composites, the electrical conductivity was not only retained but slightly increased with reinforcement content.

The electrical and thermal conductivity results are given in Table 5. The electrical resistivity measurements showed that pure copper (0% composite) had a resistivity of ~1.641×10^{-8} Ω·m, which corresponds to an electrical conductivity of about 5.56×10^{7} S/m. As the reinforcement percentage increased, the resistivity of the composites actually decreased marginally. These results indicate a clear trend: higher reinforcement led to slightly lower resistivity (slightly higher conductivity). This counter-intuitive improvement in conductivity could be explained by multiple factors. Firstly, the reduction in porosity at higher reinforcement levels increases the effective cross-sectional area for current flow [53]. This leads to reduced interparticle spacing and higher packing density, creating a tightly bonded Cu matrix. This enhanced particle contact improves the bonding and conductivity of the samples. Thus, the non-reinforced copper sample with a higher percent porosity had the lowest measured conductivity. With 10% reinforcement, porosity

was almost nil, allowing the matrix to conduct more efficiently. Also, the CuO present in the reinforcement likely undergoes reduction to metallic copper (at least partially) during the high-temperature casting process, thereby introducing finely dispersed copper regions in the matrix [34]. Alumina itself is non-conductive, but at these volume fractions (<10 vol%), its presence as tiny particles might not drastically impede the electron flow, especially if they are well enmeshed by CuO and the copper matrix. The electron mean free path in copper at room temp (~39 nm) is comparable to or smaller than the particle spacing in these composites (likely several microns apart except in clusters). Therefore, electrons can mostly circumvent the insulating particles, and as long as the matrix continuity is maintained, conductivity stays high [1]. Another possible factor is that the ceramic particles stabilize the copper matrix against structural defects that scatter electrons (such as dislocations or grain boundaries). If the composite cools in a way that results in a purer, perhaps larger-grained copper matrix (due to the presence of the oxide particles acting as grain refiners during solidification, but then reducing impurity content), the electron scattering could be reduced [51]. The net effect observed is that the introduced second phase did not harm electrical conduction. In practical terms, a conductivity of 5.85×10^7 S/m for the 10% composite means it is on par with pure copper electrically. This is a critical result because it demonstrates that one can potentially use this composite in electrical applications without sacrificing performance [19].

Table 5. Electrical and thermal conductivity results of composite samples (values are presented as averages of three replicates, n = 3).

Sample ID	Reinforcement (%)	Length (m)	Diameter (m)	Area $\times 10^{-4}$ (m^2)	Resistivity $\times 10^{-7}$ (Ωm)	Electrical Conductivity $\times 10^7$ (S/m)	Thermal Conductivity (W/mK)
A	0	0.0110	0.0140	7.917	1.641	5.56	80.55
B	2	0.0140	0.0135	8.372	1.632	5.70	80.93
C	4	0.0100	0.0140	7.477	1.630	5.73	81.70
D	6	0.0100	0.0150	8.247	1.617	5.77	82.89
E	8	0.0110	0.0130	7.147	1.601	5.82	84.50
F	10	0.0110	0.0140	7.917	1.587	5.85	105.40

When comparing relative values, the trend is important: the thermal conductivity of the composites increased with reinforcement, as shown in Table 5. The jump at 10% is notable—potentially, the 10% composite had a more efficient heat transfer path, perhaps due to minimal porosity and the formation of a continuous link between the nano-Al_2O_3 and reduced CuO filling micro-voids [38]. Similarly, in Liu et al. [54], it was found that Al_2O_3 nanostructures exhibit a synergistic effect in reducing interfacial thermal resistance and creating more compact, thermally conductive pathways through optimized particle packing in epoxy resin. In metals, thermal conductivity is largely governed by electron transport, so one would expect the thermal conductivity trend to follow the electrical conductivity trend [48]. Up to 8%, they do track (gradual increase), but at 10%, the thermal conductivity shows a disproportionately large increase. This could be due to improved heat transfer through the composite via radiative or phonon mechanisms through the oxide network at higher content [55]. However, the significant shift in the trend at 10% reinforcement may also be due to the existence of a critical volume fraction beyond which microstructural connectivity and packing efficiency change significantly or a sample-specific anomaly. Regardless, the key point is that no deterioration in thermal conduction was observed. Even with 8% reinforcement, we see a slight improvement. Thus, the composite retains the excellent heat-conducting ability of copper.

From an application standpoint, these findings are highly encouraging. They mean that the copper nanocomposite can be used in situations where electrical/thermal conductivity is paramount (such as electrical connectors and heat exchanger tubing), all while providing enhanced mechanical robustness (hardness, strength, and wear resistance) compared to pure copper [10]. This combination is rare and is the primary value proposition of this material development. One must keep in mind the scale of these improvements relative to pure copper. If the base copper was of higher purity or better processed (no porosity), perhaps the conductivity gains would not appear to be as high, but the fact remains that the composite did not introduce a significant conductivity penalty [4].

4. Conclusions

The chemical co-precipitation route produced a nanoscale mixed-oxide powder of CuO and Al_2O_3 (average crystallite size ~33.2 ± 2.4 nm). This powder, when introduced into molten copper, yielded cast composites with a fairly uniform particle distribution. The CuO/Al_2O_3 particles were effectively embedded in the copper matrix, and casting porosity was markedly reduced in the composites compared to pure copper. At higher reinforcement levels (≥8 wt%), some agglomeration of nanoparticles occurred, but overall particle–matrix interfacial bonding was good, with no large continuous defects observed. On the other hand, the addition of hard nano-oxide reinforcements led to significant improvements in the mechanical performance of copper. Brinell hardness increased steadily with reinforcement content—the 10% CuO/Al_2O_3 composite was about 2.8 times harder than pure copper. This enhanced hardness correlates with the increased wear resistance; the wear index under abrasive testing dropped by ~40% in the 10% composite relative to copper, indicating superior wear behavior. Tensile properties were also notably enhanced: the ultimate tensile strength rose from ~154 MPa (Cu) to ~260 MPa (10% composite), a ~68% increase. Impressively, this strengthening did not come at the expense of ductility—the 10% composite actually exhibited higher elongation (~43%) than the unreinforced copper (~27%). Composites with intermediate reinforcement (4–8%) showed moderate strength gains and retained ductility comparable to or slightly below that of copper, demonstrating that a judicious amount of nano-oxide can strengthen copper without embrittlement. The excellent combination of strength and ductility achieved (especially at 8–10% reinforcement) can be attributed to the uniform dispersion of nano-sized oxides, which block dislocation motion, reinforce the matrix, and reduce porosity.

There was no measurable decline in conductivity even at the highest reinforcement level; in fact, slight increases in both electrical (~5% higher than pure copper) and thermal conductivity (~5% higher up to 8%, with a larger jump at 10%) were recorded. This is likely due to the reduction in casting porosity and the potential in situ generation of metallic copper from CuO during processing, as well as the minimal disruption of electron transport by the dispersed particles. The nanocomposites thus offer the attractive benefit of mechanical reinforcement without compromising functional conductivity—an advantage over traditional copper alloys, which often see reduced conductivity with alloying additions.

The optimal performance was observed in the 8–10 wt% reinforcement range, where the improvements in mechanical properties were most pronounced. While the 10% composite gave the maximum hardness and strength, the 8% composite also provided substantial improvements with slightly less particle agglomeration. The processing method (co-precipitation of mixed oxides followed by incorporation in copper melt) proved effective for obtaining a homogeneous microstructure and good interfacial contact, which translated into superior properties.

These findings suggest that copper-based composites reinforced with ceramic nanoparticles (especially via in situ or co-precipitation routes) are a promising class of materials for advanced applications. Components like electrical connectors, electrodes, commutator segments, heat sink baseplates, or switching contacts could benefit from the improved hardness and wear resistance, enabling longer service life and better mechanical integrity under stress, all while maintaining the necessary conductivity for efficient operation. The approach of using a mixed CuO/Al_2O_3 reinforcement is particularly beneficial in addressing the wetting and dispersion challenges associated with directly adding alumina to copper.

Further investigations are recommended to optimize the processing and performance and more rigorous microstructural characterization and analysis. This includes exploring other in situ reduction processes to fully eliminate any residual CuO and thereby maximize metallic continuity, experimenting with different particle volume fractions beyond 10% to see if an optimal threshold exists, and scaling up the casting process to larger components. Additionally, studying the high-temperature behavior (creep, thermal stability) and electrical contact performance, such as under high current density, of these composites would provide insight into their suitability for real-world applications. The promising combination of properties obtained here sets a foundation for developing high-performance copper nanocomposites for electrical and thermal systems where pure copper is insufficient.

Author Contributions: V.I.A.: Investigation, Formal analysis, Writing—review and editing. O.F.A.: Writing—Original draft, Writing—review and editing, Methodology, Conceptualization, Formal analysis, Data curation. B.O.A.: Writing—Original draft, Writing—review and editing, Methodology, Data curation, Conceptualization, Methodology, Supervision, Resources, Project administration. All authors have read and agreed to the published version of the manuscript.

Funding: This research received no external funding.

Institutional Review Board Statement: Not applicable.

Data Availability Statement: The original contributions presented in this study are included in the article. Further inquiries can be directed to the corresponding author.

Acknowledgments: The authors acknowledge the Department of Metallurgical and Materials Engineering at the Federal University of Technology Akure for granting access to their laboratories.

Conflicts of Interest: The authors declare no conflicts of interest.

References

1. Liu, H.; Dong, J.; Liang, S.; Li, W.; Liu, Y. Effect of Trace Elements on the Thermal Stability and Electrical Conductivity of Pure Copper. *Coatings* **2024**, *14*, 1017. [CrossRef]
2. Dölling, J.; Henle, R.; Prahl, U.; Zilly, A.; Nandi, G. Copper-Based Alloys with Optimized Hardness and High Low-Alloyed Binary CuSc Alloys. *Metals* **2022**, *12*, 902. [CrossRef]
3. Lin, H.R.; Shao, H.; Zhang, Z.; Yang, H.; Sun, J.; Zhang, L.; Zhang, Z. Stress relaxation behaviors and mechanical properties of precipitation strengthening copper alloys. *J. Alloys Compd.* **2021**, *861*, 158537. [CrossRef]
4. Li, J.; Ding, H.; Li, B.; Wang, L. Microstructure evolution and properties of a Cu–Cr–Zr alloy with high strength and high conductivity. *Mater. Sci. Eng. A* **2021**, *819*, 141464. [CrossRef]
5. Yan, Y.F.; Kou, S.-Q.; Yang, H.-Y.; Shu, S.-L.; Qiu, F.; Jiang, Q.-C.; Zhang, L.-C. Ceramic particles reinforced copper matrix composites manufactured by advanced powder metallurgy: Preparation, performance, and mechanisms. *Int. J. Extrem. Manuf.* **2023**, *5*, 032006. [CrossRef]
6. Peng, J.H.; Binner, J.; Bradshaw, S. Microwave initiated self-propagating high temperature synthesis of materials. *Mater. Sci. Technol.* **2002**, *18*, 1419–1427. [CrossRef]
7. Gherasim, C.; Asandulesa, M.; Fifere, N.; Doroftei, F.; Tîmpu, D.; Airinei, A. Structural, Optical and Dielectric Properties of Some Nanocomposites Derived from Copper Oxide Nanoparticles Embedded in Poly(vinylpyrrolidone) Matrix. *Nanomaterials* **2024**, *14*, 759. [CrossRef]

8. Youness, R.A.; Ibrahim, M.A.; Taha, M.A. Evaluation of the electrical and dielectric behavior of the apatite layer formed on the surface of hydroxyapatite/hardystonite/copper oxide hybrid nanocomposites for bone repair applications. *Ceram. Int.* **2022**, *48*, 19837–19850. [CrossRef]
9. Ho, K.-T.; Nguyen, D.-D. Properties of Cu-Al_2O_3 Nanocomposite Materials Synthesized by Mechano-Chemical Process. *Eng. Proc.* **2025**, *111*, 5.
10. Barakat, W.S.; Habba, M.I.A.; Ibrahim, A.; Fathy, A.; Elkady, O.A. The effect of Cu coated Al_2O_3 particle content and densification methods on the microstructure and mechanical properties of Al matrix composites. *J. Mater. Res. Technol.* **2023**, *24*, 6908–6922. [CrossRef]
11. Gobalakrishnan, B.; Rajaravi, C.; Udhayakumar, G.; Lakshminarayanan, P.R. Effect of Ceramic Particulate Addition on Aluminium Based Ex-Situ and In-Situ Formed Metal Matrix Composites. *Met. Mater. Int.* **2021**, *27*, 3695–3708. [CrossRef]
12. Deschamps, I.S.; Avila, D.D.S.; Piazera, E.V.; Cruz, R.C.D.; Aguilar, C.; Klein, A.N. Design of In Situ Metal Matrix Composites Produced by Powder Metallurgy—A Critical Review. *Metals* **2022**, *12*, 2073. [CrossRef]
13. Rezayat, M.; Karamimoghadam, M.; Ashkani, O.; Bodaghi, M. Characterization and Optimization of Cu-Al_2O_3 Nanocomposites Synthesized via High Energy Planetary Milling: A Morphological and Structural Study. *J. Compos. Sci.* **2023**, *7*, 300. [CrossRef]
14. Chotai, H.; Ramani, R.V.; Markna, J.; Kataria, B. Cu and CuO Nanoparticles in Heat Transfer Applications: A Comprehensive Review. *J. Adv. Mech. Eng. Appl.* **2025**, *6*, 8–31. Available online: https://publisher.uthm.edu.my/ojs/index.php/jamea/article/view/21798 (accessed on 18 March 2026). [CrossRef]
15. Boukha, Z.; Ayastuy, J.L.; Iglesias-González, A.; Pereda-Ayo, B.; Gutiérrez-Ortiz, M.A.; González-Velasco, J.R. Preparation and characterisation of CuO/Al_2O_3 films deposited onto stainless steel microgrids for CO oxidation. *Appl. Catal. B Environ.* **2014**, *160–161*, 629–640. [CrossRef]
16. Nasiri, S.; Rabiei, M.; Palevicius, A.; Janusas, G.; Vilkauskas, A.; Nutalapati, V.; Monshi, A. Modified Scherrer equation to calculate crystal size by XRD with high accuracy, examples Fe_2O_3, TiO_2 and V_2O_5. *Nano Trends* **2023**, *3*, 100015. [CrossRef]
17. Schabikowski, M.; Stróż, A.; Kruk, A. Beyond Oxidation: Engineering Functional Anodised Metal Matrices Through Molecular and Surface Modifications. *Int. J. Mol. Sci.* **2025**, *26*, 7809. [CrossRef] [PubMed]
18. Luo, Y.; Song, X.G.; Hu, S.P.; Xu, Z.Q.; Li, Z.H.; Lei, Y. Reactive air brazing of Al_2O_3 ceramic with Ag-CuO-Pt composite fillers: Microstructure and joint properties. *J. Eur. Ceram. Soc.* **2021**, *41*, 1407–1414. [CrossRef]
19. Wang, Q.; Gao, X.; Ma, J.; Yang, S.; Ai, D.; Zhang, X.; Yue, H. A A novel electrostatic self-assembly strategy for constructing graphene/Al-Cu composites with enhanced interfacial and mechanical performance. *J. Alloys Compd.* **2025**, *1039*, 183323. [CrossRef]
20. Kleindienst, J.; Bagshaw, N.; Iten, J.; Klemm-Toole, J. Modeling Solidification Microstructure in an Inoculated Aluminum 6061 Alloy Processed with Gas Metal Arc Directed Energy Deposition. *JOM* **2025**, *77*, 1423–1437. [CrossRef]
21. Sharna, S.; Rouchon, V.; Legens, C.; Taleb, A.; Stanescu, S.; Bouillet, C.; Lambert, A.; Briois, V.; Chiche, D.; Gay, A.; et al. Role of Copper Migration in Nanoscale Ageing of Supported CuO/Al_2O_3 in Redox Conditions: A Combined Multiscale X-ray and Electron Microscopy Study. *ChemCatChem* **2023**, *15*, e202201259. [CrossRef]
22. Prasanth, G.; Madhu, G.M.; Kottam, N. Combustion Assisted Synthesis of CuO Nanoparticles and Structure-Property Evaluation in nano-CuO Polymer Composites. *Appl. Sci. Eng. Prog.* **2023**, *17*, 7259. [CrossRef]
23. Demir, M.E.; Okumuş, M. Investigation of Microhardness, Microstructural, Tribological, and Thermal Properties of Al_{7075}/TiO_2/Kaoline Hybrid Metal Matrix Composites Produced by Powder Metallurgy Process. *Adv. Eng. Mater.* **2024**, *26*, 2401343. [CrossRef]
24. Oke, S.R.; Maledi, N.; Okanlawon, I.A.; Bishi, T.R.; Falodun, O.E. Tensile and corrosion properties of copper and alumina hybrid reinforcement on aluminum matrix composite. *J. Compos. Mater.* **2025**, *59*, 1595–1607. [CrossRef]
25. Abraham, O.F.; Oloruntoba, D.T.; Sunday, A.V.; Daniel-Mkpume, C.C. Corrosion behavior of Aluminium in alkaline-water hyacinth plant extract functionalized solution: An electrochemical and weight loss study. *Chem. Data Collect.* **2023**, *43*, 100983. [CrossRef]
26. Asangi, D.U.; Chikkatti, B.S.; Sajjan, A.M.; Banapurmath, N.R.; Khan, T.Y.; Ghori, S.W.; Huddar, S.A.; Rajappa, S. Electrochemical investigation of Al_2O_3-CuO binary nanocomposite electrodes: Towards high energy storage supercapacitors. *J. Alloys Compd.* **2025**, *1029*, 180806. [CrossRef]
27. Bakke, A.O.; Arnberg, L.; Li, Y. Achieving high-strength metallurgical bonding between A356 aluminum and copper through compound casting. *Mater. Sci. Eng. A* **2021**, *810*, 140979. [CrossRef]
28. Sahoo, P.K.; Pattnaik, S.; Sutar, M.K. A State-of-the-Art Review on Manufacturing and Additive Influences on Sand-Cast Components. *Arab. J. Sci. Eng.* **2019**, *44*, 9805–9835. [CrossRef]
29. Gyarmati, G.; Erdélyi, J. Intermetallic Phase Control in Cast Aluminum Alloys by Utilizing Heterogeneous Nucleation on Oxides. *Metals* **2025**, *15*, 404. [CrossRef]

30. Dada, M.; Popoola, P. Recent advances in joining technologies of aluminum alloys: A review. *Discov. Mater.* **2024**, *4*, 86. [CrossRef]
31. Ding, X.Y.; Fu, Y.-C.; Li, B.; Lin, S.; Luo, L.-M.; Wu, Y.-C.; Yao, J.-H. Microstructure and mechanical properties of Al_2O_3 dispersion strengthened Cu by laser in-situ aluminum thermal reduction processing. *Mater. Des.* **2025**, *258*, 114547. [CrossRef]
32. Mozammil, S.; Verma, R.; Karloopia, J.; Jha, P.K. Investigation and measurement of porosity in Al + 4.5Cu/6wt%TiB_2 in situ composite: Optimization and statistical modelling. *J. Mater. Res. Technol.* **2020**, *9*, 8041–8057. [CrossRef]
33. Afifeh, M.; Hosseinipour, S.J.; Jamaati, R. Effect of post-annealing on the microstructure and mechanical properties of nanostructured copper. *Mater. Sci. Eng. A* **2021**, *802*, 140666. [CrossRef]
34. Fu, X.; Jiang, J.; Jiang, X. Research Progress in Interfacial Characteristics and Strengthening Mechanisms of Rare Earth Metal Oxide-Reinforced Copper Matrix Composites. *Materials* **2022**, *15*, 5350. [CrossRef]
35. Stavroulakis, P.; Toulfatzis, A.I.; Pantazopoulos, G.A.; Paipetis, A.S. Machinable Leaded and Eco-Friendly Brass Alloys for High Performance Manufacturing Processes: A Critical Review. *Metals* **2022**, *12*, 246. [CrossRef]
36. Abraham, O.F.; Oloruntoba, D.T.; Damilola, A.D.; Fesomade, K.I.; Ugoh, M.C.; Damilola, A.O. Electrochemical and weight loss studies of the corrosion profiles of gray cast iron under the influence of water hyacinth plant extract in 0.5 M NaOH. *Chem. Data Collect.* **2022**, *42*, 100951. [CrossRef]
37. Bharadwaj, R.; Sarkar, A.; Rakshe, B. Effect of Cooling Rate on Phase Transformation Kinetics and Microstructure of Nb–Ti Microalloyed Low Carbon HSLA Steel. *Metallogr. Microstruct. Anal.* **2022**, *11*, 661–672. [CrossRef]
38. Bao, W.; Zhang, J.; Wong, H.; Liu, J.; Li, W. Emerging Copper-to-Copper Bonding Techniques: Enabling High-Density Interconnects for Heterogeneous Integration. *Nanomaterials* **2025**, *15*, 729. [CrossRef]
39. Wang, S.; Xie, G.; Yang, J.; Liu, F.; Liu, X. Analysis of microstructure evolution and deformation mechanism of nano-oxides Al_2O_3 dispersion strengthened copper alloy during compression at room temperature. *J. Alloys Compd.* **2023**, *949*, 169837. [CrossRef]
40. Fan, Z.; Gao, F. Grain Initiation and Grain Refinement: An Overview. *Metals* **2022**, *12*, 1728. [CrossRef]
41. Bayerlein, B.; Schilling, M.; von Hartrott, P.; Waitelonis, J. Semantic integration of diverse data in materials science: Assessing Orowan strengthening. *Sci. Data* **2024**, *11*, 434. [CrossRef]
42. Mariani, M.; Bertolini, F.; Fabiocchi, L.; Mercadelli, E.; Galassi, C.; Lecis, N. Alumina-based interpenetrating phase composites by binder jetting: Effects of powder multimodal distributions on porous preforms formation and copper-infiltrated composite performance. *Mater. Charact.* **2025**, *229*, 115651. [CrossRef]
43. Tabrizi, A.T.; Aghajani, H.; Saghafian, H.; Laleh, F.F. Correction of Archard equation for wear behavior of modified pure titanium. *Tribol. Int.* **2021**, *155*, 106772. [CrossRef]
44. Lyphout, C.; Sato, K.; Houdkova, S.; Smazalova, E.; Lusvarghi, L.; Bolelli, G.; Sassatelli, P. Tribological Properties of Hard Metal Coatings Sprayed by High-Velocity Air Fuel Process. *J. Therm. Spray Technol.* **2016**, *25*, 331–345. [CrossRef]
45. Artesani, A.; Di Turo, F.; Zucchelli, M.; Traviglia, A. Recent Advances in Protective Coatings for Cultural Heritage—An Overview. *Coatings* **2020**, *10*, 217. [CrossRef]
46. Saha, G.; Valtonen, K.; Saastamoinen, A.; Peura, P.; Kuokkala, V.T. Impact-abrasive and abrasive wear behavior of low carbon steels with a range of hardness-toughness properties. *Wear* **2020**, *450–451*, 203263. [CrossRef]
47. Jones, T.D.A.; Strachan, R.; Russell, K.; Abdullah, M.; Mackie, D.M.; Cooper, M.; Frame, B.; Vorstius, J.B. Prediction of Periodic Centerline Porosity and Pulse Marks by CFD and Experimentation for Continuously Cast Copper. *Metall. Mater. Trans. B* **2023**, *54*, 499–514. [CrossRef]
48. Singh, M.K.; Gautam, R.K. Structural, Mechanical, and Electrical Behavior of Ceramic-Reinforced Copper Metal Matrix Hybrid Composites. *J. Mater. Eng. Perform.* **2019**, *28*, 886–899. [CrossRef]
49. Zhong, S.; Zhang, X.; Liu, A.; Zhang, B. Electrical and Thermal Conductivity of Graphene/Copper Composites and Their Applications in High-Efficiency Current-Carrying Conductors: A Review. *Adv. Eng. Mater.* **2025**, *27*, 2401950. [CrossRef]
50. Lee, S.H.; Chae, Y.S.; Kim, H.M.; Quach, H.L.; Kim, J.H. Investigation on characteristic of vanadium trioxide insulation mixed with metal powder for rare-earth barium copper oxide coils. *Supercond. Sci. Technol.* **2024**, *37*, 085012. [CrossRef]
51. Zhang, W.; Huang, L.; Mi, X.; Xie, H.; Feng, X.; Ahn, J.H. Researches for higher electrical conductivity copper-based materials. *cMat* **2024**, *1*, e13. [CrossRef]
52. Nemani, A.V.; Ghaffari, M.; Bokati, K.S.; Valizade, N.; Afshari, E.; Nasiri, A. Advancements in Additive Manufacturing for Copper-Based Alloys and Composites: A Comprehensive Review. *J. Manuf. Mater. Process.* **2024**, *8*, 54. [CrossRef]
53. Zhang, M.; Zhou, S.; Huang, R.; Xu, F.; Wang, J.; Dai, S.; Zhang, Y.; Zhu, L. Cold sprayed Cu-coated AlN reinforced copper matrix composite coatings with improved tribological and anticorrosion properties. *Surf. Coat. Technol.* **2025**, *496*, 131666. [CrossRef]

54. Liu, J.; Li, W.; Xu, Q.; Zhang, Y.; Niu, L.; Li, Y.; Liu, P.; Li, X.; Zhang, Z. Fabrication of multiscale alumina nanospheres for improving the thermal conductivity of epoxy resin. *Ceram. Int.* **2025**, *51*, 8138–8146. [CrossRef]
55. Danayat, S.; Mona, Z.T.; Nayal, A.S.; Annam, R.S.; Garg, J. Role of four-phonon processes in thermal conductivity of two-dimensional materials and thermal-transport enhancement arising from interconnected nanofiller networks in polymer/nanofiller composites. *Nanoscale* **2024**, *16*, 13755–13783. [CrossRef]

Disclaimer/Publisher's Note: The statements, opinions and data contained in all publications are solely those of the individual author(s) and contributor(s) and not of MDPI and/or the editor(s). MDPI and/or the editor(s) disclaim responsibility for any injury to people or property resulting from any ideas, methods, instructions or products referred to in the content.